



**HAL**  
open science

## Hidden turbulence in van Gogh's The Starry Night

Yinxiang Ma, Wanting Cheng, Shidi Huang, François G Schmitt, Xin Lin,  
Yongxiang Huang

► **To cite this version:**

Yinxiang Ma, Wanting Cheng, Shidi Huang, François G Schmitt, Xin Lin, et al.. Hidden turbulence in van Gogh's The Starry Night. *Physics of Fluids*, 2024, 36 (9), 10.1063/5.0213627 . hal-04729277

**HAL Id: hal-04729277**

**<https://hal.science/hal-04729277v1>**

Submitted on 11 Oct 2024

**HAL** is a multi-disciplinary open access archive for the deposit and dissemination of scientific research documents, whether they are published or not. The documents may come from teaching and research institutions in France or abroad, or from public or private research centers.

L'archive ouverte pluridisciplinaire **HAL**, est destinée au dépôt et à la diffusion de documents scientifiques de niveau recherche, publiés ou non, émanant des établissements d'enseignement et de recherche français ou étrangers, des laboratoires publics ou privés.

1 **Hidden Turbulence in van Gogh's *The Starry Night***

2 Yinxiang Ma (马寅翔),<sup>1</sup> Wanting Cheng (程婉婷),<sup>2</sup> Shidi Huang (黄仕迪),<sup>2</sup> François  
3 G. Schmitt,<sup>3</sup> Xin Lin (林昕),<sup>1</sup> and Yongxiang Huang (黄永祥)<sup>1,4,5</sup>

4 <sup>1</sup>*State Key Laboratory of Marine Environmental Science &*  
5 *College of Ocean and Earth Sciences, Xiamen University, Xiamen,*  
6 *China*

7 <sup>2</sup>*Center for Complex Flows and Soft Matter Research and Department of Mechanics*  
8 *and Aerospace Engineering, Southern University of Science and Technology,*  
9 *Shenzhen, Guangdong, China*

10 <sup>3</sup>*CNRS, Univ. Lille, Univ. Littoral Cote d'Opale, UMR 8187, LOG,*  
11 *Laboratoire d'Océanologie et de Géosciences, F 62930 Wimereux,*  
12 *France*

13 <sup>4</sup>*Fujian Engineering Research Center for Ocean Remote Sensing Big Data, Xiamen,*  
14 *China*

15 <sup>5</sup>*Center for Marine Meteorology and Climate Change, Xiamen University,*  
16 *Xiamen China*

17 (\*Electronic mail: yongxianghuang@{gmail.com,xmu.edu.cn})

18 (Dated: 11 October 2024)

19 Turbulent skies have often inspired artists, particularly in the iconic swirls of Vin-  
20 cent van Gogh's *The Starry Night*. For an extended period, debate has raged  
21 over whether the flow pattern in this masterpiece adheres to Kolmogorov's theory of  
22 turbulence. In contrast to previous studies that examined only part of this painting,  
23 *all and only the* whirls/eddies in the painting are taken into account in this work,  
24 following the Richardson-Kolmogorov's cascade picture of turbulence. Consequently,  
25 the luminance's Fourier power spectrum spontaneously exhibits a characteristic  $-5/3$   
26 Kolmogorov-like power-law. This result suggests that van Gogh had a very careful  
27 observation of real flows, so that not only the sizes of whirls/eddies in *The Starry*  
28 *Night* but also their relative distances and intensity follow the physical law that  
29 governs turbulent flows. Moreover, a " $-1$ "-like power-law persists in the spectrum  
30 below the scales of the smallest whirls, hinting at Batchelor-type scalar turbulence  
31 with a high Schmidt number. Our study thus unveils the hidden turbulence captured  
32 within *The Starry Night*.

## 33 I. INTRODUCTION

34 Turbulent flows or flow patterns similar to turbulence are ubiquitous in nature, rang-  
35 ing from atmospheric and oceanic flows of planetary-scale<sup>1</sup> to high-concentration bacteria  
36 suspensions at micro-scales.<sup>2,3</sup> One common feature of these phenomena is the existence of  
37 abundant swirling structures, which are also well captured by many artists and become key  
38 elements in their paintings. Examples include *The Yellow River Breaches Its Course*  
39 attributed to 13th-century Chinese artist Yuan Ma,<sup>4,5</sup> a series of drawings of water flows by  
40 Leonardo da Vinci in 1500s,<sup>1,6-9</sup> *The Great Wave off Kanagawa* by Katsushika Hoku-  
41 sai in 1831,<sup>10-12</sup> and *The Starry Night* by Vincent van Gogh in 1890,<sup>13-18</sup> to name a few.  
42 Turbulence-like patterns appearing in these artworks have inspired scientists to examine how  
43 close these patterns are to real turbulent flows. In this regard, an interesting but unsettled  
44 debate is whether the swirling structures in van Gogh's painting *The Starry Night* satisfy  
45 classical turbulence theories or not.<sup>13,15,16,19</sup>

46 To describe turbulent flows, Lewis Fry Richardson<sup>20</sup> advocated a phenomenological pic-  
47 ture in his seminal work "Weather Prediction by Numerical Process":

48 **big whirls have little whirls**  
49 **that feed on their velocity,**  
50 **and little whirls have lesser whirls**  
51 **and so on to viscosity.**

52 This cascade picture has been widely accepted for describing the kinetic energy (i.e., the  
53 square of velocity) in turbulent flows qualitatively, which is transferred from large-scale to  
54 small-scale flow structures and known as the forward energy cascade.<sup>1,4,21</sup> Later in 1941, A.N.  
55 Kolmogorov proposed his famous theory of locally homogeneous and isotropic turbulence to  
56 quantitatively characterize the Richardson's picture. According to Kolmogorov's theory,  
57 the Fourier power spectrum of kinetic energy  $E(k)$  in fully-developed turbulence follows a  
58 scaling law in the so-called inertial range  $k_L \ll k \ll k_\eta$  as,

$$59 E(k) \propto \epsilon^{2/3} k^{-5/3}, \quad (1)$$

60 where  $\epsilon$  is the mean energy dissipation rate in units of kinetic energy per unit mass and  
61 unit time; the wavenumber  $k$  is the inverse of the length scale, and the subscripts  $L$  and  
62  $\eta$  indicate the system and the Kolmogorov length scales, respectively.<sup>22</sup> This theory, now

63 recognized as the cornerstone in the field of turbulence, is the first theory to provide a  
 64 quantitative prediction of turbulent flows and has been widely verified both experimentally  
 65 and numerically.<sup>1,23,24</sup> The reader is referred to recent papers for a review of this topic.<sup>4,21</sup>

66 Note that to observe Kolmogorov's  $-5/3$  law, several requirements must be satisfied. An  
 67 important requirement is that there should be a sufficient scale separation, which could be  
 68 characterized by the Reynolds number  $\text{Re} = uL/\nu$ . Here,  $u$  is the characteristic flow velocity  
 69 and  $\nu$  is the kinematic viscosity of the fluid. This general definition of the  $\text{Re}$  number is often  
 70 interpreted as the ratio between the inertia and the viscosity forces,<sup>1,25</sup> so the Kolmogorov's  
 71  $-5/3$  law has been treated as one of the most important features of high- $\text{Re}$ -number flows  
 72 dominated by inertia forces.<sup>1,24,25</sup> Surprisingly, in recent years, turbulence-like phenomena  
 73 have been reported for low- $\text{Re}$ -number and even nearly-zero- $\text{Re}$ -number flows. These flows  
 74 include the so-called elastic turbulence,<sup>26</sup> bacterial turbulence or mesoscale turbulence,<sup>2</sup> and  
 75 lithosphere deformation,<sup>27</sup> to list a few. In these systems, despite their small  $\text{Re}$  numbers  
 76 (in the range  $\mathcal{O}(10^{-24}) \lesssim \text{Re} \lesssim \mathcal{O}(10^{-1})$ ), a wide scale separation can be still observed in  
 77 the flow patterns, and thus a turbulence-like scaling behavior emerges. These findings imply  
 78 that even for barely-flowing systems, one may examine their turbulence-like patterns in the  
 79 framework of turbulence theories.

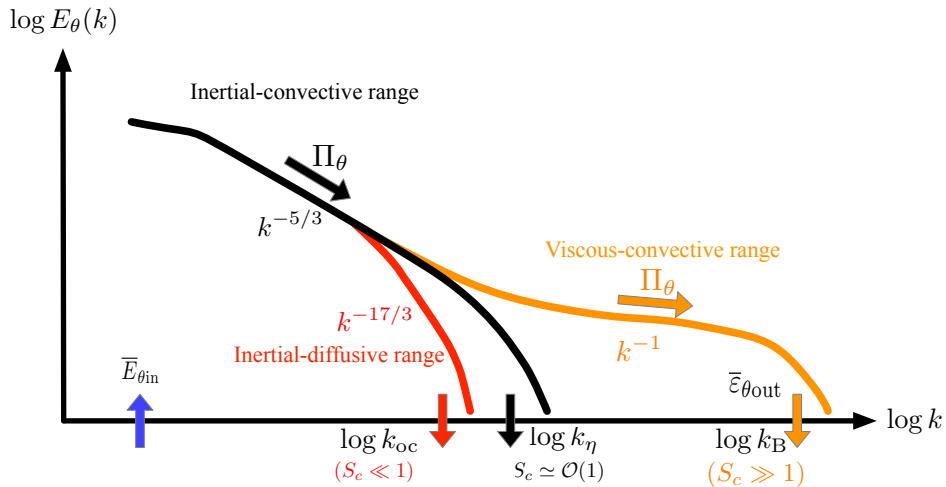


FIG. 1. Scalar spectra  $E_\theta(k)$  for different Schmidt numbers  $Sc$  reproduced from the Ref. 28. For  $Sc \gg 1$ , the so-called Batchelor spectrum  $E_\theta(k) \propto k^{-1}$  is expected to be in the range  $k_\eta \ll k \ll k_B$ , where  $k_\eta$  and  $k_B$  are the Kolmogorov and the Batchelor wavenumbers, respectively. See the text for a detailed explanation.

80 For art paintings, their patterns can be treated as snapshots of flow fields. However, one  
81 cannot obtain the kinetic energy information from these patterns. Instead, a more suitable  
82 quantity to characterize their features is luminance, which is a passive scalar similar as dye  
83 and temperature that are transported and mixed by the flow, so its spatial distribution is  
84 highly correlated to the characteristics of the velocity field. Quantitatively, the behavior of a  
85 passive scalar  $\theta$  is determined by the Schmidt number  $Sc = \nu/\kappa$ , a ratio of the fluid viscosity  
86  $\nu$  to the scalar diffusivity  $\kappa$ .<sup>23,25</sup> In terms of turbulent small-scale properties, the  $Sc$  number  
87 can also be expressed using the ratio between the Batchelor wavenumber  $k_B = (\epsilon/\nu\kappa^2)^{1/4}$   
88 of the passive scalar and the Kolmogorov wavenumber  $k_\eta = (\epsilon/\nu^3)^{1/4}$  of the velocity field:  
89  $Sc = (k_B/k_\eta)^2$ . Depending on the value of the  $Sc$  number, there exist three distinct regimes  
90 in the Fourier power spectrum of passive scalar  $E_\theta(k)$  as illustrated in Fig. 1. For  $Sc = \mathcal{O}(1)$   
91 with  $k_B \simeq k_\eta$ , a scaling behavior similar as the Kolmogorov's  $-5/3$  law can be expected in  
92 the inertial-convective subrange  $k_L \ll k \ll k_\eta$ , i.e.,

$$93 \quad E_\theta(k) = C_{OC}\epsilon_\theta\epsilon^{-1/3}k^{-5/3}, \quad (2)$$

94 where  $C_{OC}$  is the Obukhov-Corrsin constant and  $\epsilon_\theta$  is the mean scalar dissipation rate. This  
95 is the so-called Kolmogorov-Obukhov-Corrsin scaling (KOC for short).<sup>28-31</sup> For the case with  
96  $Sc \ll 1$ , one still expects the  $-5/3$  scaling, but the inertial-convective subrange is shorter  
97 than that in the KOC case since  $k_B < k_\eta$ .

98 For the case of  $Sc \gg 1$ , Batchelor<sup>32</sup> obtained the following spectrum for the scales beyond  
99 the inertial-convective subrange,

$$100 \quad E_\theta(k) = C_B\epsilon_\theta(\nu/\epsilon)^{1/2}k^{-1} \exp(-C_B(k/k_B)^2), \quad k \gg k_\eta \quad (3)$$

101 where  $C_B$  is the Batchelor constant. This shows that if  $k_B \ll k$  (i.e., in the viscous-diffusive  
102 subrange), the spectrum follows a rapid exponential decay.<sup>28,33</sup> Note that in the viscous-  
103 convective subrange, i.e.,  $k_\eta \ll k \ll k_B$ , an asymptotic power-law is expected,

$$104 \quad E_\theta(k) = C_B\epsilon_\theta(\nu/\epsilon)^{1/2}k^{-1}, \quad (4)$$

105 Several attempts have been performed to verify the Batchelor's  $-1$  scaling either experimen-  
106 tally or numerically and the evidence has become increasingly convincing in recent years.<sup>34-43</sup>  
107 However, due to the the lack of a clear scale separation, it remains challenging to observe  
108 both the KOC's  $-5/3$  scaling and the Batchelor's  $-1$  scaling simultaneously, which requires

109 at least 3~4 orders of scale separation in experiments or numerical simulations to resolve  
110 all dynamically relevant scales.<sup>28</sup>

111 Concerning the *The Starry Night* examined in the present study, it was painted by  
112 linseed oil (high fluid viscosity) mixed with stone powder (low scalar diffusivity), implying  
113 a high Sc number. Therefore, one might be curious about whether the flow pattern in  
114 this artwork adheres to the Batchelor’s theory of scalar turbulence. Aragón *et al.*<sup>13</sup> found  
115 that the increment of the luminance in this painting shows a clear scale invariance, and the  
116 corresponding probability density functions can be reproduced using the formula obtained  
117 from the turbulence theory. Beattie and Kriel<sup>15</sup> showed that the Fourier power spectrum of  
118 the luminance is close to  $E_\theta(k) \propto k^{-2}$  rather than the Kolmogorov  $-5/3$  scaling, which could  
119 be interpreted using the theory of compressible turbulence. However, Finlay<sup>16</sup> reported  
120 that the midrange wavenumber spectrum tends to obey a  $-1$  scaling. These results seem  
121 to contradict each other, partially because their examined areas of the painting were not  
122 exactly the same, so the spectrum might be contaminated by different elements in the  
123 painting. Moreover, these studies considered only part of the painting and thus some whirls,  
124 which are crucial for characterizing the multi-scale feature of turbulence, were excluded in  
125 their analysis; see Fig. 2 (b).

126 In this work, we revisit the controversial issue above by keeping *all and only* the whirls in  
127 *The Starry Night* during the analysis, following the fundamental hypothesis of Richardson-  
128 Kolmogorov’s cascade picture of turbulence. Both the Fourier power spectrum and the  
129 second-order structure function of the gray-scale luminance of the painting are analyzed.  
130 Their scaling behaviors are then compared with the prediction of the Batchelor theory of  
131 scalar turbulence. The implication of our findings will be discussed.

## 132 II. DATA AND METHOD

### 133 A. High Resolution Version of *The Starry Night*

134 *The Starry Night* is an oil-on-canvas painting by the Dutch postimpressionist painter  
135 Vincent van Gogh painted in June 1889. It depicts the view from the east-facing window of  
136 his asylum room at Saint-Rémy-de-Provence, south of France, just before sunrise, with the  
137 addition of an imaginary village and flowing sky; see Fig. 2. It has been in the permanent

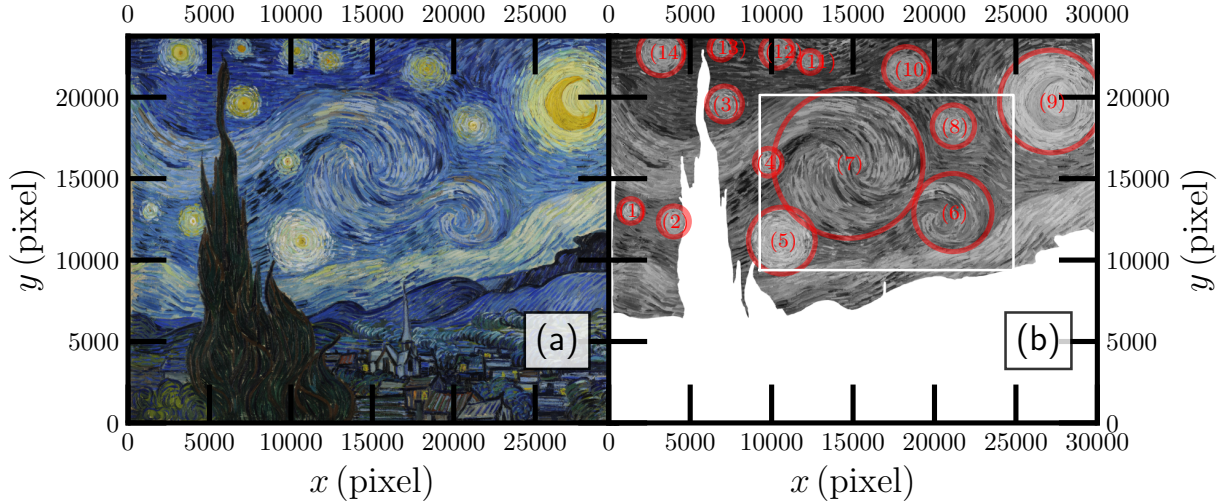


FIG. 2. (Color online) (a) a high-resolution van Gogh’s *The Starry Night* obtained from <https://artsandculture.google.com> with a size  $92.1\text{cm} \times 73.7\text{cm}$  and  $30,000\text{pixel} \times 23,756\text{pixel}$ . Visually, the sky seems to be flowing with swirling eddies. (b) Gray version of the *The Starry Night*, where the region studied by Finlay<sup>16</sup> is illustrated by a white square. The non-flow part is masked out manually. The whirls/eddies are recognized by naked eyes.

138 collection of the Museum of Modern Art in New York City since 1941, acquired through  
 139 the Lillie P. Bliss Bequest. *The Starry Night*, widely regarded as Vincent van Gogh’s  
 140 magnum opus, is one of the most recognized paintings in western art and can be widely  
 141 found in our daily life; see Fig. D.1 in the Appendix.

142 Fig.2 shows a high-resolution version of *The Starry Night* provided by Google  
 143 Art Project (<https://artsandculture.google.com>). It has a size of  $92.1\text{cm} \times 73.7\text{cm}$  and  
 144  $30,000\text{pixel} \times 23,756\text{pixel}$ , corresponding to a spatial resolution of  $30\ \mu\text{m}/\text{pixel}$ . Fourteen  
 145 eddies (including the moon) of different sizes can be recognized by naked eyes with their  
 146 diameters in the range  $4.2\text{cm} \lesssim r \lesssim 27.6\text{cm}$  (i.e.,  $1,400\text{pixel} \lesssim r \lesssim 9,200\text{pixel}$ ); see Tab. I  
 147 in the Appendix. The typical spatial scale of the brushstroke is found to be in the range  
 148  $0.09\text{cm} \lesssim r \lesssim 1.5\text{cm}$  (i.e.,  $30\text{pixel} \lesssim r \lesssim 500\text{pixel}$ ) for the width and  $1.2\text{cm} \lesssim r \lesssim 6\text{cm}$   
 149 (i.e.,  $400\text{pixel} \lesssim r \lesssim 2,000\text{pixel}$ ) for the length; see Fig. A.1 in the Appendix.

150 Before making the analysis, the original image is converted from the red-green-blue scale  
 151 to the gray-scale using the following formula,

$$Y = 0.2125R + 0.7154G + 0.0721B \quad (5)$$



153 where  $R$ ,  $G$ , and  $B$  represent the intensity for each color channel. The function `color.rgb2gray`  
 154 from the Python `scikit-image` package is utilized for this transformation, which can well pre-  
 155 serve the flow structures.<sup>44</sup> In addition, the church, mountain, and village are masked out  
 156 to exclude the potential influence of these non-flow-like elements; see Fig. 2 (b). The so-  
 157 obtained gray-scale field is subsequently treated as a passive-scalar field for the following  
 158 analysis.

## 159 B. Methods

### 160 1. *Fourier Power Spectrum*

161 As mentioned in the Introduction, when the flow is turbulent, a power-law behavior is  
 162 expected for the Fourier power spectra of both the velocity and the passive scalar advected by  
 163 the velocity field. Classically, the Fourier power spectrum is estimated using the Fast Fourier  
 164 Transform algorithm, with datasets with a size of the form  $2^p$ , where  $p$  is an integer. This  
 165 algorithm also requires datasets with no missing values. However, the masked-out data in  
 166 this work, as seen in Fig. 2 (b), have missing parts. In order to overcome these limitations, the  
 167 Fourier power spectrum is estimated via the Wiener-Khinchine theorem here. This theorem  
 168 states that, for the luminance  $\theta$  (e.g., the gray-scale field  $Y$  defined above), its Fourier power  
 169 spectrum  $E_\theta(k)$  and the autocorrelation function  $\rho_\theta(r)$  are a Fourier transform pair, which  
 170 are written as,

$$171 \quad E_\theta(k) = \int \rho_\theta(r) \exp(-j2\pi kr) dr, \quad \rho_\theta(r) = \int E_\theta(k) \exp(j2\pi kr) dk, \quad (6)$$

172 where  $j = \sqrt{-1}$  is a complex unit;  $k = 1/r$  is the wavenumber and  $r$  is the distance  
 173 between two points in the physical space. The autocorrelation function is defined as  $\rho_\theta(r) =$   
 174  $\langle \theta'(x+r)\theta'(x) \rangle$ , in which  $\theta'(x) = \theta(x) - \langle \theta \rangle$  is the scalar variation in space and  $\langle \cdot \rangle$  means  
 175 ensemble average.  $\rho_\theta(r)$  can be estimated when there are missing data, and in such case an  
 176 additional step is involved to correct the missing data effect; see detail of this algorithm in  
 177 Ref. 45. In case of scale invariance, one expects a power-law behavior of  $E_\theta(k)$  written as  
 178 below,

$$179 \quad E_\theta(k) \propto k^{-\beta_\theta}, \quad (7)$$

180 where  $\beta_\theta > 0$  is the scaling exponent that can be determined experimentally or through  
 181 theoretical considerations; for example  $\beta = 5/3$  for the velocity spectrum of high Reynolds

182 number flows.<sup>1,22,46</sup>

## 183 2. *Second-order Structure Function*

184 To characterize the scale invariance in the physical space, the second-order structure-  
185 function is often used. For luminance  $\theta$  examined here, this function is written as,

$$186 \quad S_{\theta 2}(r) = \langle \Delta_r \theta(x)^2 \rangle \propto r^{\zeta_{\theta}(2)} \quad (8)$$

187 where  $\Delta_r \theta(x) = \theta(x+r) - \theta(x)$  is the scalar increment over a distance  $r$ ;  $\zeta_{\theta}(2)$  is the second-  
188 order scaling exponent if the power-law behavior holds. A scaling relation  $\beta_{\theta} = 1 + \zeta_{\theta}(2)$   
189 is expected for  $1 < \beta_{\theta} < 3$ .<sup>1,46</sup> However, as discussed by Huang *et al.*<sup>47,48</sup>, due to several  
190 reasons, for instance, contamination by the energetic large-scale structures (e.g., ramp-cliff  
191 structures in scalar turbulence<sup>31,49</sup>), ultraviolet or infrared effects, to name a few, this scaling  
192 relation is often violated;<sup>31,47,48</sup> see more discussion in Ref.46. Note that when  $Sc \gg 1$ ,  
193 Batchelor's theory of scalar turbulence predicts a scaling value of  $\beta_{\theta} = 1$ , and the power-law  
194 in Eq. (8) is then violated due to the ultraviolet effect. For this situation, Batchelor's theory  
195 predicts a log-law, which is written as,

$$196 \quad S_{\theta 2}(r) \propto \alpha_{\theta} \ln(r) \quad (9)$$

197 where  $r_B \ll r \ll r_{\eta}$  and  $\alpha_{\theta}$  is an unknown parameter. Therefore, instead of the power-law  
198 in Eq. (8), the log-law in Eq. (9) will be tested in the present study.

## 199 III. RESULTS

### 200 A. Fourier Power Spectrum

201 The Fourier power spectra  $E_{\theta}(k)$  are estimated along the horizontal ( $x$ ) and vertical ( $y$ )  
202 directions using the algorithm described in Sec.II B 1. A bin average with 10 points per  
203 order of wavenumber is performed. Fig.3 shows the thus-obtained  $E_{\theta}(k)$ , where a dual  
204 power-law behavior is visible. As mentioned in Sec. II A, the spatial sizes of the whirles are  
205 in the range  $4.2 \text{ cm} \lesssim r \lesssim 27.6 \text{ cm}$  (i.e.,  $1,400 \text{ pixel} \lesssim r \lesssim 9,200 \text{ pixel}$ ), we therefore attempt  
206 power-law fit to the data in this range, following the Richardson-Kolmogorov's cascade  
207 picture of turbulence. It is found that power-law behaviors can be well determined in the

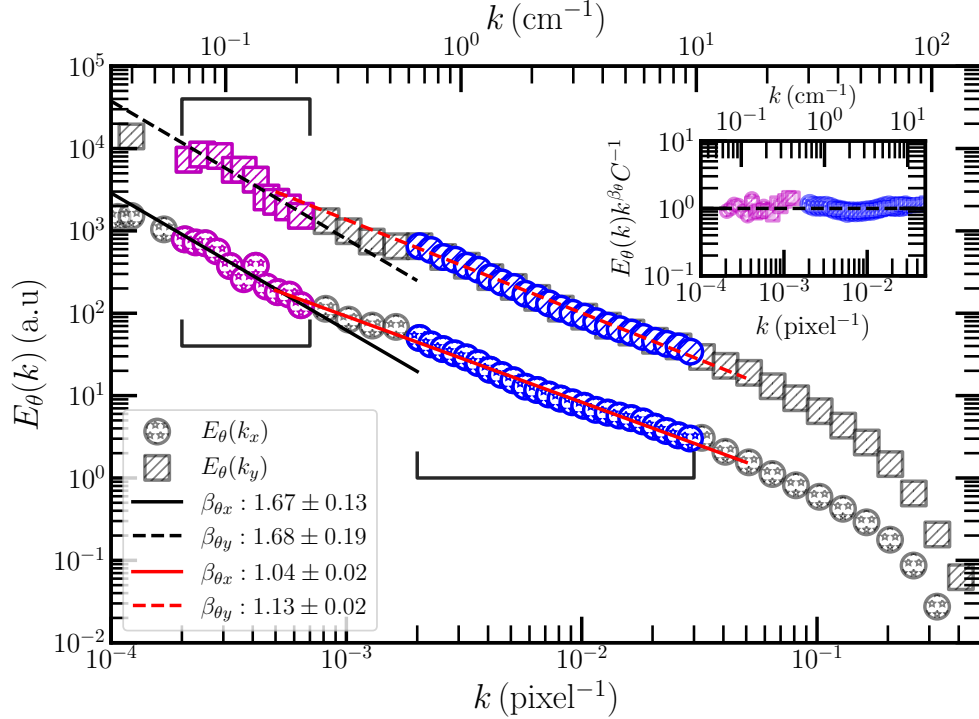


FIG. 3. (Color online) Experimental Fourier power spectrum  $E_\theta(k)$ , where the black and red lines indicate the power-law behaviors in the ranges  $6.67 \times 10^{-2} \text{ cm}^{-1} \lesssim k \lesssim 2.33 \times 10^{-1} \text{ cm}^{-1}$  (i.e.,  $2 \times 10^{-4} \text{ pixel}^{-1} \lesssim k \lesssim 7 \times 10^{-4} \text{ pixel}^{-1}$ ) and  $6.67 \times 10^{-1} \text{ cm}^{-1} \lesssim k \lesssim 10 \text{ cm}^{-1}$  (i.e.,  $2 \times 10^{-3} \text{ pixel}^{-1} \lesssim k \lesssim 3 \times 10^{-2} \text{ pixel}^{-1}$ ), respectively. For clarity, the curve  $E_\theta(k_y)$  has been shifted up by multiplying a factor of 10. The inset shows the compensated curves  $E_\theta(k)k^{\beta_\theta}C^{-1}$  using the corresponding scaling exponents  $\beta_\theta$  and prefactors  $C$  to emphasize the power-law behaviors.

208 wavenumber range  $6.67 \times 10^{-2} \text{ cm}^{-1} \lesssim k \lesssim 2.33 \times 10^{-1} \text{ cm}^{-1}$  (i.e.,  $2 \times 10^{-4} \text{ pixel}^{-1} \lesssim k \lesssim$   
 209  $7 \times 10^{-4} \text{ pixel}^{-1}$ ), corresponding to the spatial scale in the range  $4.3 \text{ cm} \lesssim r \lesssim 15 \text{ cm}$  (i.e.,  
 210  $1,430 \text{ pixel} \lesssim r \lesssim 5,000 \text{ pixel}$ ). The scaling exponents are found to be  $\beta_{\theta_x} = 1.67 \pm 0.13$   
 211 and  $\beta_{\theta_y} = 1.68 \pm 0.19$ , where the 95% fit confidence is provided by the least squares fit  
 212 algorithm. These values agree well with the one predicted by the KOC theory, since the  
 213 scaling range chosen here satisfies the requirement of the Richardson-Kolmogorov's cascade  
 214 picture of turbulence, where the whirls/eddies that cover a sufficient scale range are included  
 215 in the analysis.<sup>1,20,22,46</sup> This finding implies that the arrangement of the eddy-like formations  
 216 crafted by van Gogh resembles the energy transfer mechanism in real turbulent flows.

217 The second power-law behavior is observed in the wavenumber range  $6.67 \times 10^{-1} \text{ cm}^{-1} \lesssim$   
 218  $k \lesssim 10 \text{ cm}^{-1}$  (i.e.,  $2 \times 10^{-3} \text{ pixel}^{-1} \lesssim k \lesssim 3 \times 10^{-2} \text{ pixel}^{-1}$ ), corresponding to the spatial

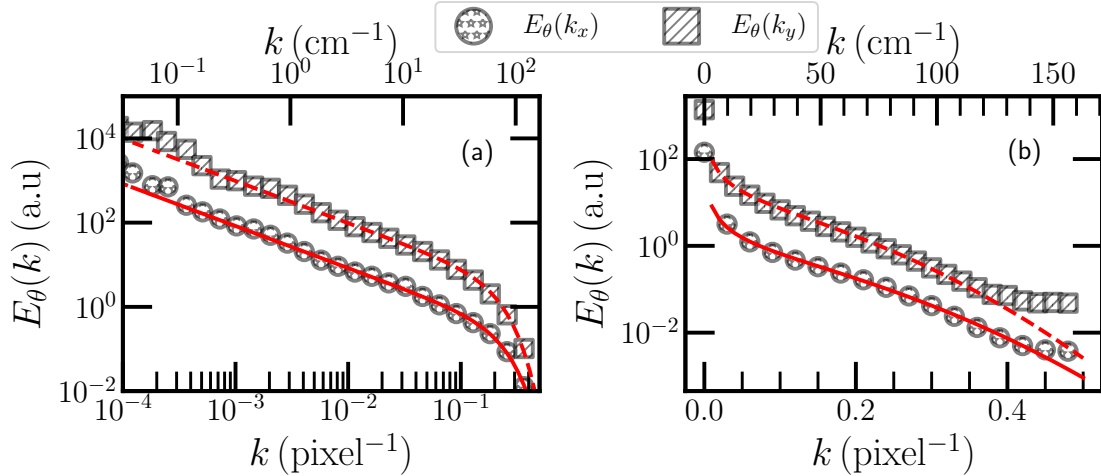


FIG. 4. (Color online) Experimental verification of Eq. (3), where the solid and dashed lines are least squares fits to the data in the range  $6.67 \times 10^{-1} \text{ cm}^{-1} \lesssim k \lesssim 1.33 \times 10^2 \text{ cm}^{-1}$  (i.e.,  $2 \times 10^{-3} \text{ pixel}^{-1} \lesssim k \lesssim 4 \times 10^{-1} \text{ pixel}^{-1}$ ) for  $E_\theta(k_x)$  and  $E_\theta(k_y)$ , respectively: (a) a log-log plot to highlight the power-law behavior  $E_\theta(k) \sim k^{-1}$ ; (b) a semilog-y plot to highlight the exponential tail  $E_\theta(k) \sim \exp\left(- (k/k_B)^2\right)$ . For clarity, the curve  $E_\theta(k_y)$  has been shifted up by a multiplying a factor of 10.

219 scale in the range  $0.1 \text{ cm} \lesssim r \lesssim 1.5 \text{ cm}$  (i.e.,  $33 \text{ pixel} \lesssim r \lesssim 500 \text{ pixel}$ ). The measured scaling  
 220 exponents are found to be  $\beta_{\theta_x} = 1.04 \pm 0.02$  and  $\beta_{\theta_y} = 1.13 \pm 0.02$ , close to the Batchelor  
 221  $-1$  scaling. As we discussed in the Introduction, such a scaling is expected to observe in the  
 222 viscous-convective range of scalar turbulence.<sup>28,37,50</sup> Notably, the wavenumber range for the  
 223  $-1$  scaling is in line with that of the brushstroke width, suggesting that the diffusion and  
 224 mixing properties associated with the painting process may result in patterns that resemble  
 225 the diffusion and mixing observed in turbulent flows.

226 To highlight the two distinct power-law behaviors, the compensated curves using the  
 227 fitted parameters are shown in Fig. 3 as inset, where clear plateaus are observed. From  
 228 Fig. 3, one can also observe a fast decay of  $E_\theta(k)$  in the large wavenumber range, motivating  
 229 us to check Eq. (3) predicted by Batchelor.<sup>32</sup> To do so, the least squares fit algorithm is  
 230 performed to the curve  $E_\theta(k)$  in the range  $6.67 \times 10^{-1} \text{ cm}^{-1} \lesssim k \lesssim 1.33 \times 10^2 \text{ cm}^{-1}$  (i.e.,  
 231  $2 \times 10^{-3} \text{ pixel}^{-1} \lesssim k \lesssim 4 \times 10^{-1} \text{ pixel}^{-1}$ ). Visually, Eq. (3) fits the data well with a Batchelor-  
 232 like parameter  $k_B = 67 \pm 6 \text{ cm}^{-1}$ , corresponding to a spatial scale of  $0.015 \text{ cm}$  (5 pixel); see  
 233 Fig. 4(a). To highlight the exponential tail  $E_\theta(k) \sim \exp\left(- (k/k_B)^2\right)$ , the results are re-

234 plotted in a semilog-y view; see Fig. 4 (b), which confirms the validation of Eq. (3).

235 **B. Second-order Structure Function**

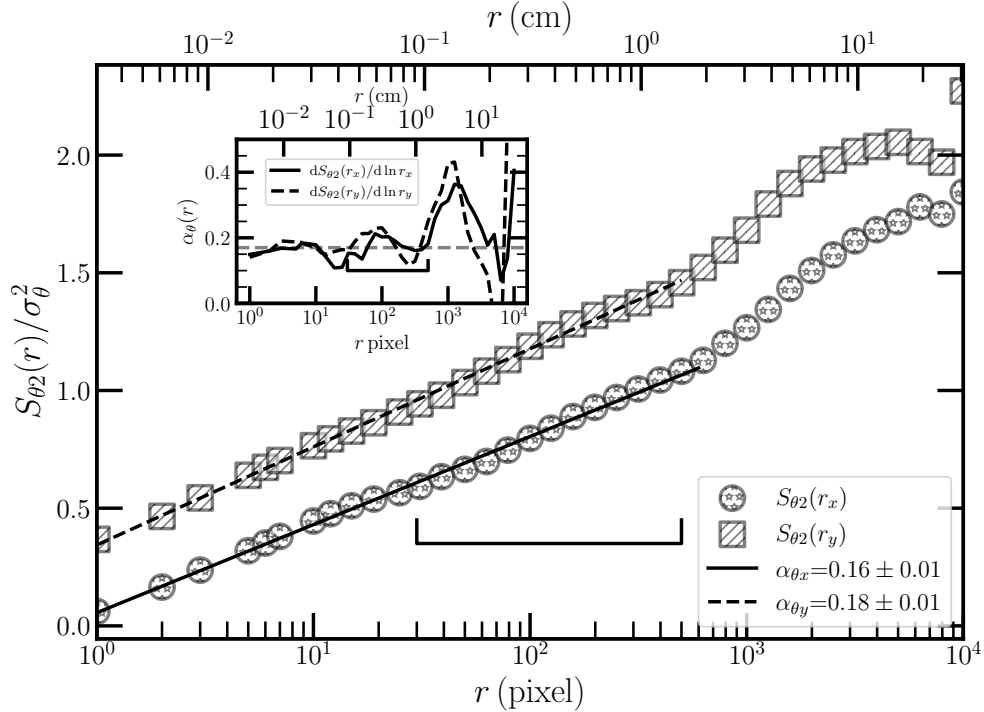


FIG. 5. (Color online) Experimental verification of Eq. (9) in a semilog-x plot, where the solid and dashed lines are least squares fit to the data in the range  $0.003 \text{ cm} \lesssim r \lesssim 1.5 \text{ cm}$  (i.e.,  $1 \text{ pixel} \lesssim r \lesssim 500 \text{ pixel}$ ) for  $S_{\theta_2}(r_x)$  and  $S_{\theta_2}(r_y)$ , respectively. For display clarity, the curve of  $S_{\theta_2}(r_y)$  has been shifted up vertically by adding a constant of 0.3. The inset shows the local slope  $\alpha_{\theta}(r) = d(S_{\theta_2}(r)/\sigma_{\theta}^2)/d \ln(r)$ , where the horizontal dash line indicates a mean value of  $\bar{\alpha}_{\theta} = 0.17 \pm 0.03$ .

236 As mentioned in Sec. II B 2, the power-law behavior of the second-order structure function  
 237 might be strongly biased due to the presence of the ultraviolet effect (e.g., the observation  
 238 of  $\beta_{\theta} \simeq 1$ ) in the present study. Therefore, instead of Eq. (8), the log-law in Eq. (9) is  
 239 examined. Fig. 5 shows the estimated second-order structure functions  $S_{\theta_2}(r)$  normalized by  
 240 the luminance variance of the examined region of the painting. A clear logarithmic law is  
 241 evident in the range  $0.003 \text{ cm} \lesssim r \lesssim 1.5 \text{ cm}$  (i.e.,  $1 \text{ pixel} \lesssim r \lesssim 500 \text{ pixel}$ ), with the fitting  
 242 slopes being  $0.16 \pm 0.01$  and  $0.18 \pm 0.01$  for the horizontal and vertical directions, respectively.  
 243 Note that this log-law range is compatible with the range of the brushstroke width. The

244 local slope  $\alpha_\theta(r) = d(S_{\theta 2}(r)/\sigma_\theta^2)/d\ln(r)$  is also estimated using a finite center difference;  
 245 see the inset in Fig. 5. Generally speaking,  $\alpha_\theta(r_x)$  and  $\alpha_\theta(r_y)$  have the same evolution trend,  
 246 with a mean value of  $\bar{\alpha}_\theta = 0.17 \pm 0.03$  in the range mentioned above. Combined with the  
 247 findings in the Fourier power spectrum, it seems that Batchelor’s scalar turbulence theory  
 248 is a good candidate for interpreting the present results phenomenologically.

## 249 IV. DISCUSSIONS

### 250 A. Turbulent Flows in Art Paintings

251 Science and art often inspire each other. To what degree the complex physics of natu-  
 252 ral flows can be captured by the patterns in artworks has attracted growing interest from  
 253 the community of fluid dynamics. For example, using a physics-informed deep learning  
 254 framework that is capable of encoding the Navier-Stokes equations into neural networks,  
 255 Raissi, Yazdani, and Karniadakis<sup>7</sup> successfully extracted the velocity and pressure fields  
 256 from Leonardo da Vinci’s painting of turbulent flows. Colagrossi *et al.*<sup>9</sup> reproduced the  
 257 physics behind one of Leonardo da Vinci’s drawings (i.e., a water jet impacts on a pool  
 258 painted in 1510-1512) by a smoothed particle hydrodynamic model, and concluded that  
 259 Leonardo da Vinci “was able to extract essential phenomena of complex air-water flows and  
 260 accurately describe each flow feature independently of the others, both in his drawings and  
 261 in their accompanying notes”. In fact, Leonardo da Vinci is considered one of the pioneers  
 262 in identifying the characteristic feature of turbulent flows, as evidenced by the multi-scale  
 263 eddies pattern depicted in several of his artworks.<sup>5,6,8</sup>

264 Concerning *The Starry Night* painted by Vincent van Gogh, our results show a clear  
 265 evidence of the  $-5/3$  scaling law when all and only the whirls/eddies in the painting are  
 266 included in the analysis. According to the Richardson-Kolmogorov’s cascade picture of  
 267 turbulence, a sufficient number of eddies with a wide distribution of scales should be involved  
 268 to observe the  $-5/3$  scaling; see more examples in the Appendix C. Our present finding thus  
 269 suggests that, not only the size distribution of whirls/eddies in *The Starry Night* but also  
 270 their relative distance and intensity follow the physical law that governs the behaviors of  
 271 turbulent flows. In other words, Vincent van Gogh had a very careful observation of real  
 272 flows, and the  $-5/3$  scaling observed here is due to this excellent mimic of real flows.

273 **B. Estimation of the Reynolds and the Schmidt numbers**

274 As previously noted, the Richardson-Kolmogorov  $-5/3$  scaling requires a wide range of  
 275 scales, usually associated with high Reynolds number flows. The  $-5/3$  scaling revealed here  
 276 arises from the artist's representation of real flows, as opposed to the nonlinear interactions  
 277 between multi-scale eddies in hydrodynamic turbulence. Meanwhile, the  $-1$  scaling could  
 278 result from physical processes like diffusion and mixing during painting. According to the  
 279 Batchelor's theory of scalar turbulence, one should have a stationary flow with the Schmidt  
 280 number  $Sc \gg 1$  to observe the  $-1$  scaling.<sup>32</sup> The former condition is automatically satisfied,  
 281 since the flows during preparing the painting oil and the painting process are slow enough.  
 282 The latter condition is arguably satisfied, as *The Starry Night* was painted by linseed  
 283 oil (high fluid viscosity) mixed with stone powder (low scalar diffusivity). To check these  
 284 conditions quantitatively, we estimate the Reynolds and the Schmidt numbers as follows.

285 As mentioned in Sec. II A, the length of the brushstroke is in the range  $1.2 \text{ cm} \lesssim r \lesssim$   
 286  $6 \text{ cm}$ . We therefore take the median value, that is  $L = 3.6 \text{ cm}$ , as the characteristic length  
 287 scale. Assuming that the typical time scale for each brushstroke is 1 sec, then the typical  
 288 velocity during the painting is around  $u \simeq 3.6 \text{ cm/s}$ . Therefore, the Reynolds number is  
 289 estimated to be  $Re = uL/\nu_{\text{eff}} \simeq 19.1 \propto \mathcal{O}(10)$ , where  $\nu_{\text{eff}} \simeq 6.79 \times 10^{-5} \text{ m}^2/\text{s}$  is the effective  
 290 kinematic viscosity estimated by the Einstein relation approximately; see Appendix B for  
 291 the estimation in detail.<sup>51</sup>

292 Note that the Reynolds number can also be expressed as the separation ratio of the  
 293 characteristic scales in turbulent flows,<sup>23</sup> i.e.,

$$294 \quad Re \propto \left( \frac{L_E}{\eta_k} \right)^{4/3} \quad (10)$$

295 where  $L_E$  represents the size of the largest eddy and  $\eta_k$  is the Kolmogorov dissipation  
 296 scale. In the present study, we can estimate the value of  $L_E$  from the painting, being  
 297  $L_E \simeq 27.6 \text{ cm}$  approximately. For the value of  $\eta_k$ , Fig. 3 shows that the  $-5/3$  scaling and  
 298 the Batchelor-like scaling are observed in the spatial scale ranges  $4.3 \text{ cm} \lesssim r \lesssim 15 \text{ cm}$   
 299 and  $0.1 \text{ cm} \lesssim r \lesssim 1.5 \text{ cm}$ , respectively; so  $\eta_k$  should lie between 1.5 cm and 4.3 cm. Then  
 300 the Reynolds number estimated from Eq.(10) is in the range  $11.9 \lesssim Re \lesssim 48.6$ , which is  
 301 also  $\mathcal{O}(10)$  and consistent with the value estimated above. The Taylor microscale Reynolds  
 302 number can be further calculated using the well-known formula  $Re_\lambda = \left( \frac{20}{3} Re \right)^{1/2}$ <sup>23</sup>, resulting

303 in a range  $9 \lesssim \text{Re}_\lambda \lesssim 18$ .

304 As for the Schmidt number, its value can be calculated by  $\text{Sc} = (k_B/k_\eta)^2 = (\eta_k/\eta_B)^2$ . The  
305 Batchelor-like scale  $\eta_B$  has been obtained from Fig. 4, which is  $\eta_B \simeq 0.015$  cm. And since  
306  $1.5 \text{ cm} \lesssim \eta_k \lesssim 4.3 \text{ cm}$  as discussed above, the low bound of the Schmidt number is estimated  
307 to be  $\text{Sc} \simeq (1.5/0.015)^2 = \mathcal{O}(10^4)$ . Alternatively, the Schmidt number can be approximated  
308 by using its original definition:  $\text{Sc} = \nu_{\text{eff}}/\kappa_{\text{eff}} = \mathcal{O}(10^{11})$ , where  $\nu_{\text{eff}} \simeq 6.79 \times 10^{-5} \text{ m}^2/\text{s}$   
309 and  $\kappa_{\text{eff}} \simeq 3.90 \times 10^{-16} \text{ m}^2/\text{s}$  are the effective kinematic viscosity and diffusivity coefficient  
310 estimated using the Einstein relation; refer to Appendix B for details. Both estimation  
311 methods yield a value of  $\text{Sc} \gg 1$ . Therefore, the requirement for Batchelor's theory of scalar  
312 turbulence is satisfied.

### 313 C. Batchelor Scalar Turbulence

314 As mentioned in the Introduction, the prediction of the Batchelor's theory of scalar turbu-  
315 lence is difficult to realize not only in experiments but also in numerical simulations.<sup>28</sup> Several  
316 attempts have been made to verify this theory. For example, Amarouchene and Kellay<sup>38</sup> ob-  
317 served Batchelor scaling for the thickness fluctuation of fast-flowing soap films. However, to  
318 fit the experiment spectrum curve, instead of Batchelor's original proposal  $k^{-1} \exp(-k/k_B)^2$ ,  
319 an exponential tail is considered, that is,  $k^{-1} \exp(-k/k_B)$ , the form proposed by Kraichnan<sup>52</sup>  
320 when the fluctuation of the strain is taken into account. Here, we can fit the experimental  
321 curve using Batchelor's original proposal, since the basic assumption of his theory of scalar  
322 turbulence is satisfied.

323 Numerically, Clay<sup>50</sup> has examined the asymptotic behavior of the Batchelor's prediction  
324 via direct numerical simulations of isotropic turbulence at  $\text{Re}_\lambda \simeq 140$  with  $4 \lesssim \text{Sc} \lesssim 512$ .  
325 It is found that with increasing the Sc number, a wider range of scales is developed in the  
326 scalar field, resulting in a more pronounced  $-1$  scaling in the Fourier power spectrum  $E_\theta(k)$ .  
327 In this context, one may anticipate that the Batchelor's  $-1$  scaling could be attainable at a  
328 lower Reynolds number with a larger Schmidt number. Indeed, Yeung *et al.*<sup>37</sup> have observed  
329 a Batchelor-like scalar spectrum at  $\text{Re}_\lambda \simeq 8$  by increasing the Sc number from 64 to 1024,  
330 which is close to the values of  $\text{Re}_\lambda$  and Sc numbers estimated in the present study and thus  
331 provides a support of our finding.

332 It is important to highlight two recent notable studies of scalar turbulence.<sup>41,43</sup> Iwano *et al.*<sup>41</sup>



333 conducted a turbulent jet experiment with a Schmidt number  $Sc \simeq 3,000$  and a Reynolds  
 334 number  $Re_\lambda \simeq 200$ . Dye concentration was measured at a fixed point using an optical  
 335 fiber LIF (laser-induced fluorescence) probe with a spatial resolution of  $2.8 \mu\text{m}$ . Utiliz-  
 336 ing Taylor’s frozen hypothesis,<sup>1,53</sup> the observed six-order magnitude of wavenumber power  
 337 spectra indicated the coexistence of Kolmogorov and Batchelor scalings. However, as  
 338 He, Jin, and Yang<sup>53</sup> noted, the application of Taylor’s frozen hypothesis should be ap-  
 339 proached with caution. Saito, Watanabe, and Gotoh<sup>43</sup> conducted a direct numerical simu-  
 340 lation of the passive scalar under a special setup, where the passive scalar was carried by  
 341 particles in isotropic turbulence to achieve large Schmidt numbers with a Reynolds number  
 342 as high as  $Re_\lambda \simeq 500$ . Their Fourier power spectra provided clear evidence of the coexistence  
 343 of Kolmogorov  $-5/3$  scaling and Batchelor  $-1$  scaling over a scale range of one order of  
 344 magnitude for each. Nonetheless, simultaneous observation of Kolmogorov’s  $-5/3$  scaling  
 345 and Batchelor’s  $-1$  scaling through direct experimental measurements in the spatial domain  
 346 remains challenging. The findings of the present study may inspire experimental approaches  
 347 like “painting in turbulent flows” to address this issue in the future.

## 348 V. CONCLUSION

349 In summary, we show in this work that when all eddies in the painting is considered  
 350 in the analysis, the turbulence-like statistics can be recovered for the *The Starry Night*,  
 351 with a Kolmogorov  $-5/3$  scaling corresponding to the multi-scale eddies represented by the  
 352 painter, and a Batchelor  $-1$  scaling produced by the oil of the painting, corresponding to  
 353 the viscous-convective range. In other words, Vincent van Gogh, as one of the most notable  
 354 post-impressionist painters, had a very careful observation of turbulent flows: he was able  
 355 to reproduce not only the size of whirls/eddies, but also their relative distance and intensity  
 356 in his painting. Furthermore, the full Batchelor spectrum (i.e., Eq. (3)) is found for spatial  
 357 scales below the size of the eddies. This is because during the preparation of the painting  
 358 oil and the drawing process, the characteristic Reynolds number is low and the diffusivity is  
 359 dominant. This is nicely confirmed by the second-order structure function which precisely  
 360 follows the theoretical prediction, showing a log-law. This study thus reveals the hidden  
 361 turbulence in the painting *The Starry Night* using both Kolmogorov’s and Batchelor’s  
 362 theories.

## 363 ACKNOWLEDGMENTS

364 The authors express their gratitude to Mr. Fulian Gan, Ms. Ruoyi Xie, Ms. Xuan Lei,  
365 and Ms. Xiangying Li for providing us with their photographs. This work is sponsored by  
366 the National Natural Science Foundation (Nos. 12102165 and U22A20579).

## 367 AUTHOR DECLARATIONS

## 368 CONFLICT OF INTEREST

369 The authors have no conflicts to disclose.

## 370 AUTHOR CONTRIBUTIONS

371 **Y.X. Huang:** Conceptualization (lead); Formal analysis (lead); Investigation (lead);  
372 Writing - review & editing (lead). **Y.X. Ma:** Formal analysis (supporting); Methodol-  
373 ogy (supporting). **S.D. Huang:** Investigation (supporting); Writing - review & editing  
374 (supporting). **W.T. Cheng:** Formal analysis (supporting); Investigation (supporting). **X.**  
375 **Lin:** Investigation (supporting); Writing - review & editing (supporting). **F.G. Schmitt:**  
376 Investigation (supporting); Writing - review & editing (supporting).

## 377 VI. DATA AVAILABILITY

378 The data that support the findings of this study are available at <https://artsandculture.google.com>,  
379 <https://www.tate.org.uk> and <https://www.planetary.org>. A copy of the source code for the  
380 present analysis is available at <https://github.com>.

## 381 **Appendix A: Typical Spatial Scales**

382 The detection of the scaling range should follow the requirement of turbulence theories,  
383 that is, there should be enough whirling structures involved in the statistics. Here, we  
384 manually estimate the typical spatial scale for both visualized whirls and brush strokes.

### 385 **1. Spatial Scales of Whirls**

386 The spatial sizes of fourteen whirls/eddies are estimated by naked eyes. Their diameters,  
387 locations, and areas are listed in Tab. I. Following Richardson's picture of turbulent energy  
388 cascade, the Kolmogorov  $-5/3$  scaling is expected in the range  $1,400 \text{ pixel} \lesssim r \lesssim 9,200 \text{ pixel}$   
389 (i.e.,  $4.2 \text{ cm} \lesssim r \lesssim 27.6 \text{ cm}$ ), corresponding to a wavenumber range  $1 \times 10^{-4} \text{ pixel}^{-1} \lesssim k \lesssim$   
390  $7 \times 10^{-4} \text{ pixel}^{-1}$  (i.e.,  $3 \times 10^{-2} \text{ cm}^{-1} \lesssim k \lesssim 2 \times 10^{-1} \text{ cm}^{-1}$ ). Two distinct types of structures  
391 can be visually distinguished. The first type resembles an eddy with a ring-shaped pattern,  
392 while the other one is spiral in nature; see Fig. A.1.

### 393 **2. Spatial Scales of Brushstrokes**

394 The spatial scales of the brushstrokes are estimated manually with the width and  
395 length around  $30 \text{ pixel}$  and  $500 \text{ pixel}$  (i.e.,  $0.09 \text{ cm} \lesssim r \lesssim 1.5 \text{ cm}$ ) and around  $400 \text{ pixel}$   
396 and  $2,000 \text{ pixel}$  (i.e.,  $1.2 \text{ cm} \lesssim r \lesssim 6 \text{ cm}$ ), respectively. Fig. A.1 shows an example of three  
397 typical whirls/eddies. The Batchelor's  $-1$  scaling law is expected in these ranges.

TABLE I. Geometric properties of eddies in *The Starry Night* manually checked by naked eyes. The diameters of the whirls/eddies are roughly in the range 1,400 pixel  $\sim$  9,200 pixel (i.e., 4.2 cm  $\sim$  27.6 cm), corresponding to a scale ratio around  $\simeq$  6.6. The Kolmogorov-like  $-5/3$  scaling law is expected in this range.

No.	$D$ (pixel/cm)	location x (pixel)	location y (pixel)	area (pixel <sup>2</sup> /cm <sup>2</sup> )
1	1,500/4.5	1,268	12,987	1,767,146/15.9
2	1,900/5.7	3,926	12,320	2,835,287/25.5
3	2,200/6.6	7,015	19,662	3,801,327/34.2
4	1,700/5.1	9,721	15,973	2,269,801/20.4
5	4,100/12.3	10,549	11,114	13,202,543/118.8
6	4,800/14.4	20,998	12,857	18,095,573/162.9
7	9,200/27.6	14,625	15,861	66,476,101/598.3
8	2,600/7.8	21,070	18,235	5,309,292/47.8
9	6,300/18.9	27,113	19,718	31,172,453/280.1
10	2,800/8.4	18,180	21,795	6,157,522/55.4
11	1,400/4.2	12,279	22,129	1,539,380/13.9
12	2,000/6.0	10,230	22,759	3,141,593/28.3
13	1,500/4.5	6,762	23,074	1,767,146/15.9
14	2,800/8.4	3,076	22,722	6,157,522/55.4

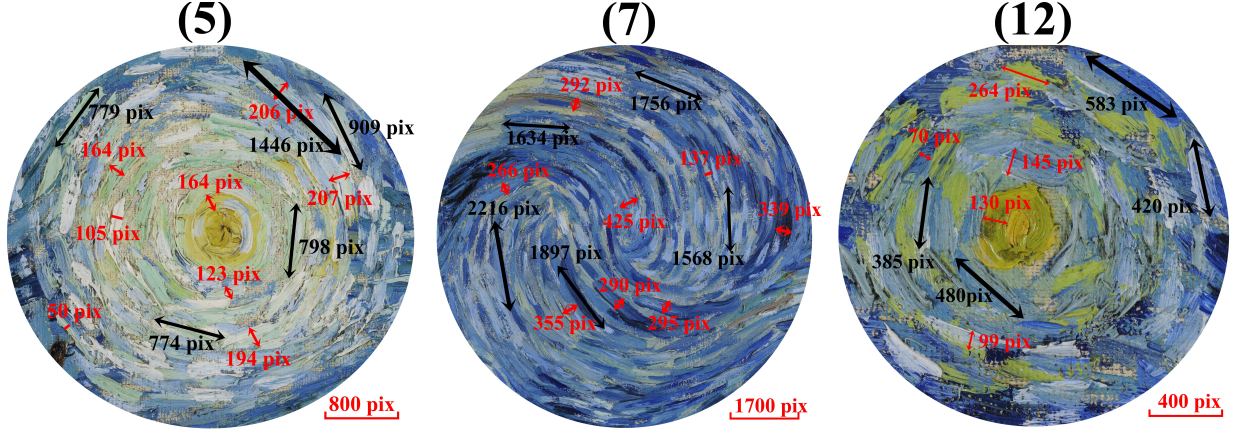


FIG. A.1. (Color online) Typical spatial scales of brushstrokes for the Nos. (5), (7) and (12) eddies marked in Fig. 2 of the main text. The width (red line) and length (black line) are found roughly in the range  $30 \text{ pixel} \lesssim r \lesssim 500 \text{ pixel}$  (i.e.,  $0.09 \text{ cm} \lesssim r \lesssim 1.5 \text{ cm}$ ) and  $400 \text{ pixel} \lesssim r \lesssim 2,000 \text{ pixel}$  (i.e.,  $1.2 \text{ cm} \lesssim r \lesssim 6 \text{ cm}$ ), respectively. The variation of the luminance in this range is thought to be caused by the preparation of painting oil and diffusion of the solid particles.

398 **Appendix B: The Effective Kinematic Viscosity and Diffusivity Estimated**  
 399 **From Kinematic Dynamics**

400 *The Starry Night* is an oil-on-canvas painting by Vincent van Gogh in 1889. At that  
 401 time, the painting oil was made of stone powder and linseed oil. Using the classical knowl-  
 402 edge of the thermal dynamics, the effective kinematic viscosity can be roughly estimated as  
 403 follows.

404 Concerning stone powder in linseed oil, we can use a model called the Einstein equation  
 405 to estimate its effective kinematic viscosity,<sup>54</sup> which is written as,

$$406 \quad \mu_{\text{eff}} = \mu_f(1 + 2.5\phi), \quad (\text{B1})$$

407 where  $\mu_{\text{eff}}$  is the effective dynamic viscosity of the suspension,  $\mu_f$  is the dynamic viscosity  
 408 of the fluid, and  $\phi$  is the volume fraction of the particles in the suspension. It is an empiri-  
 409 cal relationship that relates the effective viscosity of a suspension to the properties of the  
 410 particles and the fluid. When combining the mass ratio of stone powder and linseed oil as  
 411 1 : 1,<sup>55</sup> the effective viscosity is then,

$$412 \quad \mu_{\text{eff}} = \mu_f \left(1 + 2.5 \frac{\rho_f}{\rho_f + \rho_s}\right), \quad (\text{B2})$$

413 Substituting the given dynamic viscosity of linseed oil  $\mu_f = 0.055 \text{ Pa} \cdot \text{s}$  at the room temper-  
 414 ature, that is  $T = 293.15 \text{ K}$ , the density of linseed oil  $\rho_f = 0.93 \text{ g/cm}^3$ , the density of stone  
 415  $\rho_s = 2.5 \text{ g/cm}^3$ , we get,

$$416 \quad \mu_{\text{eff}} = 1.68\mu_f = 9.24 \times 10^{-2} \text{ Pa} \cdot \text{s}, \quad (\text{B3})$$

417 The effective kinematic viscosity is then estimated as,

$$418 \quad \nu_{\text{eff}} = \frac{\mu_{\text{eff}}}{\rho_{\text{eff}}} \simeq 6.79 \times 10^{-5} \text{ m}^2/\text{s}, \quad (\text{B4})$$

419 where the effective fluid density is calculated as  $\rho_{\text{eff}} \simeq 1360 \text{ kg/m}^3$ .

420 It is important to note that the previously mentioned estimated Reynolds number is  
 421 approximately  $\mathcal{O}(10)$ . Therefore, the Einstein equation condition may not hold. In this  
 422 context, considering the order of the Reynolds number, a more precise effective kinematic  
 423 viscosity does not alter our conclusion.

424 Moreover, the diffusion coefficient of a spherical particle in a liquid can be estimated  
 425 using the Stokes-Einstein equation,<sup>51</sup> which is written as,

426

$$\kappa_{\text{eff}} = \frac{k_{\text{Bol}}T}{6\pi\mu_f r}. \quad (\text{B5})$$

427

428

429

430

431

432

433

434

Here,  $k_{\text{Bol}} = 1.38 \times 10^{-23} \text{m}^2 \text{kg} \text{s}^{-2} \text{K}^{-1}$  is the Boltzmann constant;  $T$  is the absolute temperature;  $\mu_f$  is the dynamic viscosity of the liquid; and  $r$  is the radius of the spherical particle. We estimate here an order of the Schmidt number; therefore, we do not consider a nonspherical particle or a mixture of particle sizes where more complex models may be required. Taking into account an average particle radius of  $r = 10 \mu\text{m}$  and a dynamic viscosity of the linseed oil at room temperature, that is,  $\mu_f = 0.055 \text{Pa} \cdot \text{s}$ , the mass diffusivity of the stone powder in the linseed oil can be estimated to be around  $\kappa_{\text{eff}} \simeq 3.90 \times 10^{-16} \text{m}^2/\text{s}$ . Finally, we have an estimation of Schmidt number as,

435

$$\text{Sc} = \frac{\nu_{\text{eff}}}{\kappa_{\text{eff}}} \simeq 1.74 \times 10^{11} = \mathcal{O}(10^{11}) \quad (\text{B6})$$

436

437

438

439

This value is above the value of the low bound estimated from Fourier power spectrum. It is important to note that the above estimation assumes that the particles are small enough so that they do not interact with each other, which may not be the case for more concentrated suspensions or for particles with complex shapes.

440 **Appendix C: Examination of Additional Images**

441 In this section, we examine two additional images, respectively, the painting *Chain Pier,*  
 442 *Brighton* by John Constable in 1826 and Jupiter Great Red Spot by Voyage 1 on 5 March  
 443 1979. The same analysis as for *The Starry Night* is performed. The Kolmogorov-like  
 444  $-5/3$  power spectra are evident since the turbulence-like pattern is well maintained in these  
 445 two images.

446 **1. *Chain Pier, Brighton* by John Constable**

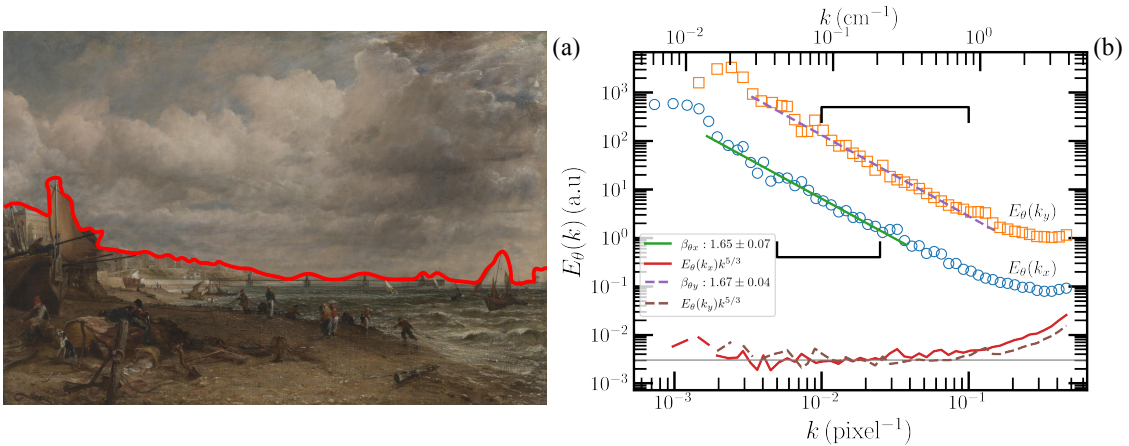


FIG. C.1. (a) *Chain Pier, Brighton* painted by John Constable in 1827, obtained from <https://www.tate.org.uk>. The land and the cloud sky is separated by the red line. (b) Experimental Fourier power spectrum  $E_\theta(k)$  of *Chain Pier, Brighton*. The green and purple dashed lines indicate power-law behaviors in the range  $5 \times 10^{-3} \text{ pixel}^{-1} \lesssim k \lesssim 2.5 \times 10^{-2} \text{ pixel}^{-1}$  (i.e.,  $4.2 \times 10^{-2} \text{ cm}^{-1} \lesssim k \lesssim 2.1 \times 10^{-1} \text{ cm}^{-1}$ ) and  $10^{-2} \text{ pixel}^{-1} \lesssim k \lesssim 10^{-1} \text{ pixel}^{-1}$  (i.e.,  $8.3 \times 10^{-2} \text{ cm}^{-1} \lesssim k \lesssim 8.3 \times 10^{-1} \text{ cm}^{-1}$ ) for the data in the horizontal and vertical directions, respectively. For display clarity, the curve of  $E_\theta(k_y)$  has been shifted up vertically by multiplying a factor of 10. The red solid and brown dashed lines are compensated curves  $E_\theta(k)k^{5/3}$  to highlight the  $-5/3$  scaling.

447 John Constable (11 June 1776 to 31 March 1837) was an English landscape artist associ-  
 448 ated with the Romantic tradition. He is primarily recognized for transforming the landscape  
 449 painting genre. He conducted many observational studies of landscapes and clouds, aim-



450 ing to be more scientific in capturing atmospheric conditions. The impact of his physical  
451 effects was often evident even in the large-scale paintings he displayed in London. The  
452 *Chain Pier, Brighton* is one such painting, completed in 1826 and shown in 1827, in which  
453 the cloud/sky and beach/land are well separated. Unlike *The Starry Night*, this paint-  
454 ing lacks well-defined swirling patterns, but the clouds are rich of structures with different  
455 scales, resembling those frequently seen in the sky; see Fig. C 1 (a).

456 A digital version of *Chain Pier, Brighton* can be accessed from <https://www.tate.org.uk>.  
457 The dimensions of the image are 183 cm  $\times$  127 cm, equivalent to 1,536 pixel  $\times$  1,057 pixel,  
458 with a spatial resolution of approximately 0.12 cm/pixel. The original image is converted  
459 to gray-scale and treated as a scalar field. The Fourier power spectrum  $E_\theta(k)$  for both  
460 horizontal ( $x$ ) and vertical ( $y$ ) directions is then calculated after excluding the land area,  
461 as shown in Fig. C 1 (a). It is not surprising that the Kolmogorov-like  $-5/3$  spectrum is  
462 evident in Fig. C 1 (b) for both  $E_\theta(k_x)$  and  $E_\theta(k_y)$ , as Constable accurately captured the  
463 cloud patterns.

## 464 2. Jupiter Great Red Spot by Voyage 1

465 The Great Red Spot is a long-lasting high-pressure area in Jupiter's atmosphere, creat-  
466 ing the largest anticyclonic storm in the Solar System. It is the most distinctive feature on  
467 Jupiter, characterized by its red-orange hue. Situated 22 degrees south of Jupiter's equator,  
468 it generates wind speeds up to 432 km/h. The Jupiter's Great Red Spot rotates counter-  
469 clockwise with a period of approximately 4.5 Earth days with roughly 16,400 km in width,  
470 making it 1.3 times the diameter of Earth. The storm has persisted for centuries due to the  
471 absence of a solid planetary surface to create friction; gas eddies in the atmosphere continue  
472 for extended periods because there is no resistance to their angular momentum.<sup>56</sup>

473 A high-resolution image of the Great Red Spot can be found at <https://www.planetary.org>,  
474 with dimensions of 7,400 pixel  $\times$  5,550 pixel and a spatial resolution of approximately  
475 6 km/pixel. Captured by Voyager 1 on 5 March 1979, the image was taken using a green  
476 and violet filter mosaic with its narrow angle camera (NAC), covering the majority of the  
477 Great Red Spot. To highlight various details, the image's color, contrast, and sharpness  
478 have been enhanced. It is the highest resolution color data available for Jupiter before the  
479 Juno mission. A square region with a size of 7,300 pixel  $\times$  5,050 pixel was cropped from the

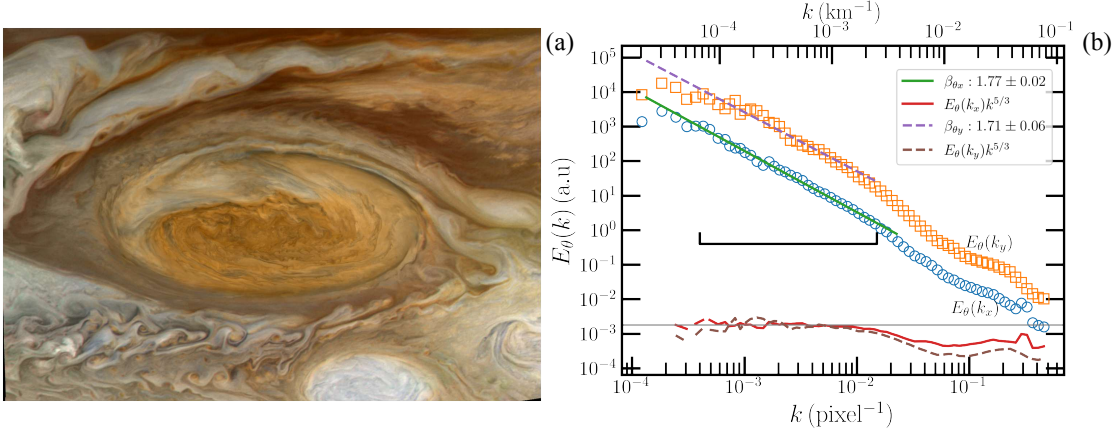


FIG. C.2. (a) *The Great Red Spot* obtained from <https://www.planetary.org> with a cropped size of 7,300 pixel  $\times$  5,050 pixel. Courtesy of NASA/JPL-Caltech/Björn Jónsson. (b) Experimental Fourier power spectrum  $E_\theta(k)$ , in which the green and purple dashed lines indicate power-law behaviors in the range  $4 \times 10^{-4} \text{ pixel}^{-1} \lesssim k \lesssim 1.5 \times 10^{-2} \text{ pixel}^{-1}$  (i.e.,  $6.7 \times 10^{-5} \text{ km}^{-1} \lesssim k \lesssim 2.5 \times 10^{-3} \text{ km}^{-1}$ ) for the data in horizontal and vertical directions, respectively. For display clarity, the curve of  $E_\theta(k_y)$  has been shifted vertically by multiplying a factor of 10. The red solid and brown dashed lines are compensated curves  $E_\theta(k)k^{5/3}$  to highlight the  $-5/3$  scaling.

480 original by excluding the black edges of original stitched photo; see Fig. C.2 (a). Visually, the  
 481 Great Red Spot shows an ellipse-like pattern approximately with a major axis of 4,000 pixel  
 482 and a minor axis of 2,000 pixel, corresponding to 24,000 km and 12,000 km. In addition to  
 483 the Great Red Spot, very rich eddy-like structures can be seen, ranging in size from 50 pixel  
 484 to 2,000 pixel, corresponding to 300 km to 12,000 km.

485 The raw image is converted to gray-scale and considered as a scalar field. The Fourier  
 486 power spectrum  $E_\theta(k)$  for both the horizontal ( $x$ ) and vertical ( $y$ ) directions is depicted in  
 487 Fig. C.2 (b). The Kolmogorov-like  $-5/3$  spectrum is apparent in the range  $4 \times 10^{-4} \text{ pixel}^{-1} \lesssim$   
 488  $k \lesssim 1.5 \times 10^{-2} \text{ pixel}^{-1}$  (i.e.,  $6.7 \times 10^{-5} \text{ km}^{-1} \lesssim k \lesssim 2.5 \times 10^{-3} \text{ km}^{-1}$ ) in both horizontal  
 489 and vertical directions. It is important to note that this scaling range aligns well with the  
 490 measured spatial size of the eddy-like structures; see Fig. C.2 (a). Similarly to our obser-  
 491 vations for *The Starry Night*, both the spatial distribution and the relative intensity of  
 492 these eddy-like structures adhere to the Richardson-Kolmogorov cascade picture. Here, the  
 493 Kolmogorov-like  $-5/3$  spectrum spontaneously emerged due to hydrodynamic interactions  
 494 between different eddies.

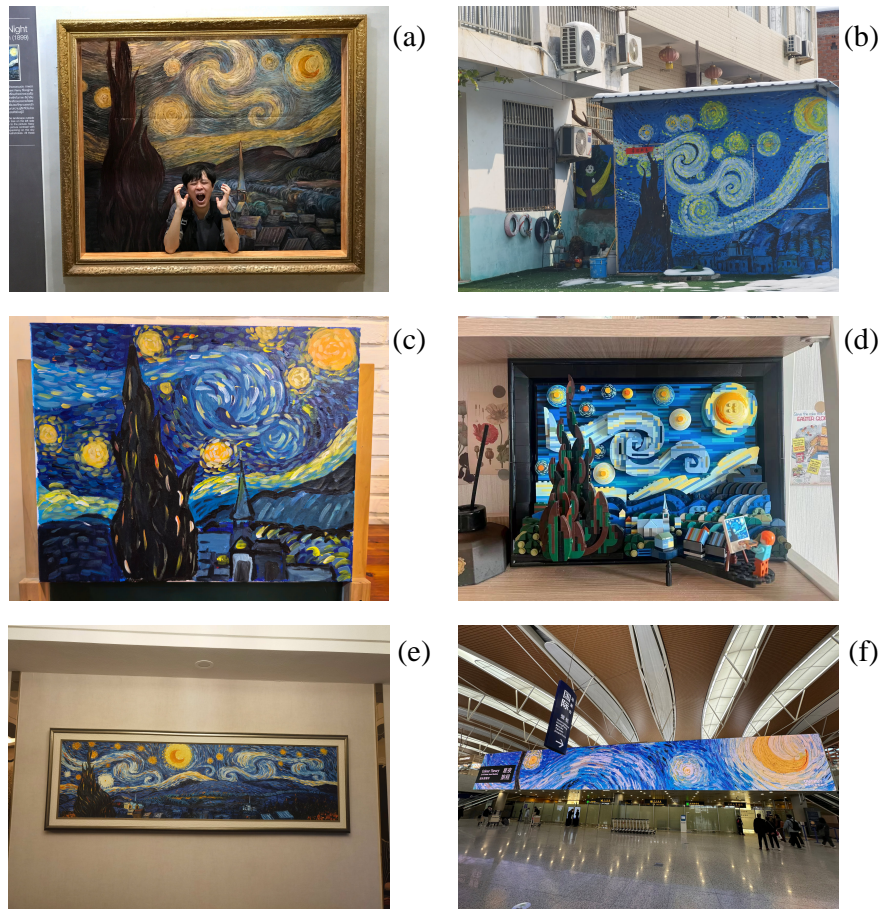


FIG. D.1. (Color online) Incorporating van Gogh’s *The Starry Night* into everyday life. (a) A man with a reproduction of *The Starry Night* during an exhibition in Pattaya, Thailand. Photographed by X.L. on 19 February 2018. (b) A picture of *The Starry Night* adorns the wall of a kindergarten in Randeng, a small town located in Fengyang County, Anhui Province, China. Photographed by Y.H. on 7 February 2024. (c) A practice painting of *The Starry Night* by a 9-year-old girl, Ruoyi Xie on 2 August 2021. Photographed by X.L. in Fuzhou, Fujian Province, China, on 16 March 2024. (d) An image of a LEGO<sup>®</sup> jigsaw puzzle depicting *The Starry Night*. Photographed by Ms. Xuan Lei in Shenzhen, Guangdong Province, China, on 24 March 2024. (e) *The Starry Night* graces a family home in Jiuquan, Gansu Province, China. Photographed by Ms. Xiangying Li, Jiuquan, Gansu Province, China, on 16 March 2024. (f) *The Starry Night* on an advertisement board at the Pudong International Airport, Shanghai, China. Photographed by Mr. Fulian Gan on 7 April 2024.

496 *The Starry Night* frequently appears in our everyday lives. Several instances are illus-  
497 trated in Fig. D.1. For instance, Fig. D.1 (a) shows an exhibition in Pattaya, Thailand, during  
498 Ms. X.L.'s visit on 19 February 2018. She captured this image with her husband standing in  
499 front of the replicated *The Starry Night*. In Fig. D.1 (b), a reproduced *The Starry Night*  
500 decorates the wall of a kindergarten in Randeng, a small town in Fengyang County, Anhui  
501 Province, China, during Y.H.'s attendance at his niece's wedding on 7 February 2024. *The*  
502 *Starry Night* is also cherished by children. For example, Fig. D.1 (c) showcases a prac-  
503 tice piece by a 9-year-old girl, Ms. Ruoyi Xie, on 2 August 2021. Meanwhile, Ms. Xuan  
504 Lei used a LEGO<sup>©</sup> jigsaw puzzle version of *The Starry Night* to embellish her room in  
505 Shenzhen, Guangdong Province, China; see Fig. D.1 (d). Several thousand kilometers from  
506 Shenzhen, Ms. Xiangying Li also selected a reproduced *The Starry Night* to beautify her  
507 family home in Jiuquan, Gansu Province, China; see Fig. D.1 (e). It is fascinating to ob-  
508 serve *The Starry Night* on an advertising board at the Pudong International Airport and  
509 Hongqiao International Airport, Shanghai, China; see Fig. D.1 (f). This advertisement pro-  
510 motes the artist Mr. Jesse Woolston's exhibition in Shanghai, China since the Mid-Autumn  
511 Festival, 10 September 2022. Mr. Woolston created a series of stunning works inspired  
512 by *The Starry Night* and physics, which can be found at <https://www.youtube.com> and  
513 <https://www.tiktok.com>.

514 We believe more examples can be found worldwide. We hope that the work showcased  
515 here will inspire the younger generation to participate in fundamental research, as sparking  
516 curiosity through captivating artwork is a crucial approach for advancing scientific progress.  
517 Finally, we would like to quote the words directly from Ref. 18:

518 "We argue that although art has no systematic conventions for conveying knowl-  
519 edge in the way science does, the arts often play an important epistemic role in  
520 the production and understanding of scientific knowledge. We argue for what we  
521 call weak scientific cognitivism, the view that the production and distribution of  
522 scientific knowledge can benefit from engagement with art."

523 **REFERENCES**

- 524 <sup>1</sup>U. Frisch, *Turbulence: the legacy of AN Kolmogorov* (Cambridge University Press, 1995).
- 525 <sup>2</sup>H. H. Wensink, J. Dunkel, S. Heidenreich, K. Drescher, R. E. Goldstein, H. Löwen, and  
526 J. M. Yeomans, “Meso-scale turbulence in living fluids,” *Proc. Natl. Acad. Sci.* **109**, 14308–  
527 14313 (2012).
- 528 <sup>3</sup>X. Qiu, L. Ding, Y. Huang, M. Chen, Z. Lu, Y. Liu, and Q. Zhou, “Intermittency mea-  
529 surement in two-dimensional bacterial turbulence,” *Phys. Rev. E* **93**, 062226 (2016).
- 530 <sup>4</sup>Y. Zhou, “Turbulence theories and statistical closure approaches,” *Phys. Rep.* **935**, 1–117  
531 (2021).
- 532 <sup>5</sup>Z. Warhaft, “The art of turbulence,” *Am. Sci.* **110**, 360–367 (2022).
- 533 <sup>6</sup>G. Chen, S. Yang, and N. Jiang, “Leonardo da Vinci and fluid mechanics,” *Mech. Eng.* (in  
534 Chinese) **41**, 634–639 (2019).
- 535 <sup>7</sup>M. Raissi, A. Yazdani, and G. E. Karniadakis, “Hidden fluid mechanics: Learning velocity  
536 and pressure fields from flow visualizations,” *Science* **367**, 1026–1030 (2020).
- 537 <sup>8</sup>I. Marusic and S. Broomhall, “Leonardo da Vinci and fluid mechanics,” *Ann. Rev. Fluid*  
538 *Mech.* **53**, 1–25 (2021).
- 539 <sup>9</sup>A. Colagrossi, S. Marrone, P. Colagrossi, and D. Le Touzé, “Da Vinci’s observation of  
540 turbulence: A French-Italian study aiming at numerically reproducing the physics behind  
541 one of his drawings, 500 years later,” *Phys. Fluids* **33**, 115122 (2021).
- 542 <sup>10</sup>J. H. Cartwright and H. Nakamura, “What kind of a wave is hokusai’s great wave off  
543 kanagawa?” *Notes Rec. Roy. Soc.* **63**, 119–135 (2009).
- 544 <sup>11</sup>J. M. Dudley, V. Sarano, and F. Dias, “On Hokusai’s great wave off Kanagawa: Local-  
545 ization, linearity and a rogue wave in sub-Antarctic waters,” *Notes Rec. Roy. Soc.* **67**,  
546 159–164 (2013).
- 547 <sup>12</sup>S. Ornes, “Science and culture: Dissecting the great wave,” *Proc. Natl. Acad. Sci.* **111**,  
548 13245–13245 (2014).
- 549 <sup>13</sup>J. L. Aragón, G. G. Naumis, M. Bai, M. Torres, and P. K. Maini, “Turbulent luminance  
550 in impassioned van Gogh paintings,” *J. Math. Imaging Vision* **30**, 275–283 (2008).
- 551 <sup>14</sup>D. W. Olson, *Celestial Sleuth: Using Astronomy to Solve Mysteries in Art, History and*  
552 *Literature* (Springer, 2014).
- 553 <sup>15</sup>J. Beattie and N. Kriel, “Is the Starry Night turbulent?” arXiv (2019),

554 10.48550/arXiv.1902.03381.

555 <sup>16</sup>W. H. Finlay, “The midrange wavenumber spectrum of van Gogh’s Starry Night does not  
556 obey a turbulent inertial range scaling law,” *J. Turbul.* **21**, 34–38 (2020).

557 <sup>17</sup>M. L. Spreafico and E. Tramuns, “The Starry Night among art, maths, and origami,” *J.*  
558 *Math. Arts* **15**, 1–18 (2021).

559 <sup>18</sup>A. Sherman and D. Anderson, “How art contributes to scientific knowledge,” *Philos. Psy-*  
560 *chol.* **36**, 1–21 (2023).

561 <sup>19</sup>K. Wright, “Arts & culture: Turbulence in the starry night,” (2019).

562 <sup>20</sup>L. Richardson, *Weather prediction by numerical process* (Cambridge University Press,  
563 1922).

564 <sup>21</sup>A. Alexakis and L. Biferale, “Cascades and transitions in turbulent flows,” *Phys. Rep.*  
565 **767-769**, 1–101 (2018).

566 <sup>22</sup>A. N. Kolmogorov, “Local structure of turbulence in an incompressible fluid at very high  
567 Reynolds numbers,” *Dokl. Akad. Nauk SSSR* **30**, 301 (1941).

568 <sup>23</sup>S. Pope, *Turbulent Flows* (Cambridge University Press, 2000).

569 <sup>24</sup>A. Tsinober, *An informal conceptual introduction to turbulence* (Springer Verlag, 2009).

570 <sup>25</sup>H. Tennekes and J. L. Lumley, *A First Course in Turbulence* (MIT Press, 1972).

571 <sup>26</sup>A. Groisman and V. Steinberg, “Elastic turbulence in a polymer solution flow,” *Nature*  
572 **405**, 53–55 (2000).

573 <sup>27</sup>X. Jian, W. Zhang, Q. Deng, and Y. Huang, “Turbulent lithosphere deformation in the  
574 Tibetan Plateau,” *Phys. Rev. E* **99**, 062122 (2019).

575 <sup>28</sup>K. R. Sreenivasan, “Turbulent mixing: A perspective,” *Proc. Natl. Acad. Sci.* **116**, 18175–  
576 18183 (2019).

577 <sup>29</sup>A. M. Obukhov, “Structure of the temperature field in a turbulent flow,” *Izv. Acad. Nauk*  
578 *SSSR Ser. Geog. Geofiz* **13**, 58–69 (1949).

579 <sup>30</sup>S. Corrsin, “On the spectrum of isotropic temperature fluctuations in an isotropic turbu-  
580 lence,” *J. Appl. Phys.* **22**, 469–473 (1951).

581 <sup>31</sup>Z. Warhaft, “Passive scalars in turbulent flows,” *Annu. Rev. Fluid Mech.* **32**, 203–240  
582 (2000).

583 <sup>32</sup>G. K. Batchelor, “Small-scale variation of convected quantities like temperature in turbu-  
584 lent fluid part 1. general discussion and the case of small conductivity,” *J. Fluid Mech.* **5**,  
585 113–133 (1959).

- 586 <sup>33</sup>D. A. Donzis, K. Sreenivasan, and P. Yeung, “The Batchelor spectrum for mixing of passive  
587 scalars in isotropic turbulence,” *Flow Turbul. Combust.* **85**, 549–566 (2010).
- 588 <sup>34</sup>C. Gibson and W. Schwarz, “The universal equilibrium spectra of turbulent velocity and  
589 scalar fields,” *J. Fluid Mech.* **16**, 365–384 (1963).
- 590 <sup>35</sup>X. Wu, B. Martin, H. Kellay, and W. Goldburg, “Hydrodynamic convection in a two-  
591 dimensional Couette cell,” *Phys. Rev. Lett.* **75**, 236–239 (1995).
- 592 <sup>36</sup>R. Antonia and P. Orlandi, “Effect of Schmidt number on small-scale passive scalar tur-  
593 bulence,” *Appl. Mech. Rev.* **56**, 615–632 (2003).
- 594 <sup>37</sup>P. Yeung, S. Xu, D. Donzis, and K. Sreenivasan, “Simulations of three-dimensional turbu-  
595 lent mixing for Schmidt numbers of the order 1000,” *Flow Turbul. Combust.* **72**, 333–347  
596 (2004).
- 597 <sup>38</sup>Y. Amarouchene and H. Kellay, “Batchelor scaling in fast-flowing soap films,” *Phys. Rev.*  
598 *Lett.* **93**, 214504 (2004).
- 599 <sup>39</sup>P. Götzfried, M. S. Emran, E. Villermaux, and J. Schumacher, “Comparison of Lagrangian  
600 and Eulerian frames of passive scalar turbulent mixing,” *Phys. Rev. Fluids* **4**, 044607  
601 (2019).
- 602 <sup>40</sup>M. Mohaghar, L. P. Dasi, and D. R. Webster, “Scalar power spectra and turbulent scalar  
603 length scales of high-Schmidt-number passive scalar fields in turbulent boundary layers,”  
604 *Phys. Rev. Fluids* **5**, 084606 (2020).
- 605 <sup>41</sup>K. Iwano, J. Hosoi, Y. Sakai, and Y. Ito, “Power spectrum of high Schmidt number scalar  
606 in a turbulent jet at a moderate Reynolds number,” *Exp. Fluids* **62**, 129 (2021).
- 607 <sup>42</sup>J. Bedrossian, A. Blumenthal, and S. Punshon-Smith, “The Batchelor spectrum of passive  
608 scalar turbulence in stochastic fluid mechanics at fixed Reynolds number,” *Comm. Pure*  
609 *Appl. Math.* **75**, 1237–1291 (2022).
- 610 <sup>43</sup>I. Saito, T. Watanabe, and T. Gotoh, “Spectrum of passive scalar carried by particles in  
611 isotropic turbulence,” *Phys. Rev. Fluids* **9**, 054601 (2024).
- 612 <sup>44</sup>We conducted the same analysis for each individual channel (not shown here). Apart from  
613 the blue channel, the Fourier power spectra of the red and green channels exhibited the  
614 same  $-5/3$  and  $-1$  scalings as found from the gray-scale field, indicating that the flow-like  
615 structures are well maintained.
- 616 <sup>45</sup>Y. Gao, F. G. Schmitt, J. Y. Hu, and Y. X. Huang, “Scaling analysis of the China France  
617 Oceanography SATellite along-track wind and wave data,” *J. Geophys. Res. Oceans* **126**,

618 e2020JC017119 (2021).

619 <sup>46</sup>F. G. Schmitt and Y. Huang, *Stochastic Analysis of Scaling Time Series: From Turbulence*  
620 *Theory to Applications* (Cambridge University Press, 2016).

621 <sup>47</sup>Y. Huang, F. Schmitt, Z. Lu, P. Fougairolles, Y. Gagne, and Y. Liu, “Second-order struc-  
622 ture function in fully developed turbulence,” *Phys. Rev. E* **82**, 026319 (2010).

623 <sup>48</sup>Y. Huang, L. Biferale, E. Calzavarini, C. Sun, and F. Toschi, “Lagrangian single particle  
624 turbulent statistics through the Hilbert-Huang Transforms,” *Phys. Rev. E* **87**, 041003(R)  
625 (2013).

626 <sup>49</sup>Y. Huang, F. Schmitt, J.-P. Hermand, Y. Gagne, Z. Lu, and Y. Liu, “Arbitrary-order  
627 Hilbert spectral analysis for time series possessing scaling statistics: Comparison study  
628 with detrended fluctuation analysis and wavelet leaders,” *Phys. Rev. E* **84**, 016208 (2011).

629 <sup>50</sup>M. P. Clay, *Strained turbulence and low-diffusivity turbulent mixing using high perfor-*  
630 *mance computing*, Ph.D. thesis, Georgia Institute of Technology (2017).

631 <sup>51</sup>A. Einstein, “On the movement of particles suspended in resting liquids required by the  
632 molecular kinetic theory of heat,” *Ann. Phys.* **322**, 549–560 (1905).

633 <sup>52</sup>R. H. Kraichnan, “Small-scale structure of a scalar field convected by turbulence,” *Phys.*  
634 *Fluids* **11**, 945–953 (1968).

635 <sup>53</sup>G. He, G. Jin, and Y. Yang, “Space-time correlations and dynamic coupling in turbulent  
636 flows,” *Annu. Rev. Fluid Mech.* **49**, 51–70 (2017).

637 <sup>54</sup>A. Einstein, “Eine neue bestimmung der moleküldimensionen,” *Ann. Phys.* **4**, 289–306  
638 (1906).

639 <sup>55</sup>We estimate here the order of Schmidt number, therefore the value of this ratio does not  
640 change our conclusion.

641 <sup>56</sup>J. H. Rogers, “The accelerating circulation of Jupiter’s Great Red Spot,” *J. Br. Astron.*  
642 *Assoc.* **118**, 14–20 (2008).